AIAA 93-0873

Viscous Flow Computations of Flow Field around an Advanced Propeller

T.B.Lim and Lakshmi N. Sankar
School of Aerospace Engineering
Georgia Institute of Technology
Atlanta, GA

31st Aerospace Sciences Meeting & Exhibit
January 11-14, 1993 / Reno, NV

AIAA-93-0873

Viscous Flow Computations of Flow field around an Advanced Propeller

T. B. Lim*, Lakshmi N. Sankar**
School of Aerospace Engineering
Georgia Institute of Technology
Atlanta, GA 30332-0150

ABSTRACT

An existing inviscid Euler analysis capable of solving the inviscid compressible flow and the aeroelastic response of advanced propeller has been recently modified to handle viscous flow. The results of viscous flow calculations for the advanced SR7L configuration are reported in the present work. The results are in good agreement with experimental data. The calculations obtained are able to capture several important flow features such as the formation and roll-up of blade tip vortices and secondary radial flow over the blade surface.

INTRODUCTION

The prediction of flow features over a highly loaded propeller is a very interesting, complex and important problem, which has constantly challenged many aerodynamicists. Even in the relatively simple case of axial flight at zero angle of attack, several interesting phenomena occur, such as the formation of curved tip vortices, leading edge vortices and radial centrifugally pumped flows. Moreover, modern high speed propellers are often designed to have a high leading edge sweep and thin airfoils at the blade tip to delay the onset of transonic flow and to reduce compressibility losses, noise. Such propellers deform readily under aerodynamic loading. The elastic deformation in turn influences the aerodynamic loading on the blade. The aerodynamic and aeroelastic characteristics are tightly coupled, which makes the prediction of flow field around the blade a difficult job.

The simple Goldstein [1] strip analysis uses potential theory to model the propeller as a straight lifting line vortex and its wakes as a solid rigid helical vortex sheet. Improvements have been made to this analysis by Sullivan[2] and Egolf [3] through the use of a curved lifting line and wake vortex filaments to account for blade sweep and nacelle influence. Other works based on potential flow theory include the finite volume approach of Jou [4] who solved the compressible full potential equation, and the linearized analysis of Hanson [5] and Williams [6] which solved for the blade pressure distribution by means of a lifting surface approach.

Numerical studies on propfan's flowfield based on the Euler equations have also been done by many researchers. Chaussee [7,8] and Bober [9,10] have developed a fully implicit finite difference NASPROP code to solve for steady state inviscid solution. Nallasammy [11] modified an explicit fine volume turbomachinery code developed by Denton [12] to obtain steady state inviscid solution. The above codes use explicitly added numerical viscosity to treat the convective flux terms. Whitfield, in his works [13,14] to calculate unsteady solution for single rotating as well as counter-rotating propfan, used Roe's flux formulation, which is naturally dissipative, with post-processing to extend the basic first order Roe flux to higher order of accuracy. The analysis by Srivastava and Sankar [15], on which the present work is based, solves for the inviscid aerodynamic loading on the blade and the resulting aeroelastic response. Using an iterative method, Srivastava et al. coupled the structural deformation computations done using NASTRAN with the Euler results to obtain the steady state blade deformation and flow field around a single rotating propfan as well as a counter-rotating propfan.

Matsuo et al [16] and Hall et al [17] have recently solved the full Navier Stokes equations for propfan configurations. The present method is an improvement over the excellent work of Matsuo et al. in that it uses state of the art upwind schemes to model inviscid terms and numerical viscosity. The method documented by Hall is an explicit time marching scheme, which restricts it primarily to steady flows because of time step constraint that will be encountered in unsteady flow calculation. The present work uses an implicit time marching scheme, which makes it more suitable for steady flows (present work), and future unsteady aeroelastic applications such as transonic or stall flutter. Furthermore, since this work is an extension of the earlier aeroelastic analysis of Srivastava et. al., this solver can be used to study aeroelastic phenomena such as divergence, stall flutter etc.

* Graduate Student, Member AIAA
** Professor, Senior Member AIAA

The objectives of the present work are: (a) Incorporation of viscous effects into the existing Euler analysis for high speed propellers, (b) Improvements to the robustness and convergence characteristics of the flow solver using modern upwind schemes, and isotropically scaled non-linear dissipation schemes, and (c) investigation of viscous flow phenomena such as tip vortex formation and the effects of centrifugal forces on the radial flow over the blade.

The present formulation uses the Reynold's mass averaged Navier-Stokes equation in a fully conservative form. The spatial derivatives are discretized using second order central differencing (CD scheme) or a third order Roe type of differencing (ROE scheme), while the temporal derivatives are treated with first order Euler implicit scheme. In order to reduce the computer memory and CPU time required to invert three block tridiagonal matrix equations present in most of the existing fully implicit formulations [18,19], a hybrid scheme is used that treats the radial or spanwise convective flux semi-explicitly and the other two convective fluxes implicitly. This hybrid scheme requires only two inversions of block tridiagonal matrices and requires the flow variables to be stored only at one time level.

MATHEMATICAL AND NUMERICAL FORMULATION

The 3-D unsteady, compressible Reynolds-averaged Navier-Stokes equations may formally be written as

$$q_t + F_x + G_y + H_z = R_x + S_y + T_z \qquad (1)$$

Here q is vector containing the unknown flow properties such as density, velocity and temperature. The quantities F, G and H are inviscid flux vectors and contain information related to the convective transport of mass, momentum and energy and pressure forces. The terms R, S and T contain viscous (laminar and turbulent) stress contributions to mass, momentum and energy transport.

To facilitate the computation of flow past arbitrary shaped configurations such as propellers and center bodies, and to account for the propeller rotation these equations are transformed to a new coordinate system (ξ,η,ζ,τ), in which the solid surfaces such as the wing or fuselage maps on to surfaces such as ζ= constant or ξ= constant. In such a coordinate system, the governing equations may formally be written as

$$\mathbf{q}_\tau + \mathbf{F}_\xi + \mathbf{G}_\eta + \mathbf{H}_\zeta = \mathbf{R}_\xi + \mathbf{S}_\eta + \mathbf{T}_\zeta \qquad (2)$$

The quantities $\mathbf{q}$, $\mathbf{F}$, $\mathbf{G}$, $\mathbf{H}$ etc. depend on their Cartesian counterparts q, F, G and H through the metrics of transformation.

The objective of calculation is then to integrate these equations numerically, starting from an initial guess for the flow vector q, by marching in time. The initial condition used here is the impulse condition. At every time step, appropriate boundary conditions for the flow properties must be imposed. In viscous flows, the appropriate boundary conditions for the solid fluid interface are the velocity no slip conditions and the disappearance of the temperature and density gradient. Conditions at the farfield boundaries away from solid body are computed by extrapolating the non-reflecting characteristic variables in the proper direction upon inflow or outflow. In addition for the axi-symmetrical rotating flow, the radial equilibrium need to be applied at outflow farfield. At the inter passage boundary, as steady state solution is sought, the periodicity condition need to be applied so as to allow the numerical domain to be confined to a single passage thereby drastically reduce the grid size required.

A finite difference procedure has been used to approximate the various derivatives appearing in equation (2). Although second order accuracy and fourth order accuracy in space are possible with the present formulation, for the sake of clarity only the simplest first order temporal-second order spatial formulation is described here. The finite difference analog of equation (2) at a time level 'n' is then

$$\Delta\mathbf{q}^{n+1}/\Delta\tau + \delta_\xi \mathbf{F}^{n+1} + \delta_\eta \mathbf{G}^{*} + \delta_\zeta \mathbf{H}^{n+1} = (\delta_\xi \mathbf{R} + \delta_\eta \mathbf{S} + \delta_\zeta \mathbf{T})^n \qquad (3)$$

Here δ_ξ , δ_η and δ_ζ are standard symmetric central difference operators. The quantity $\Delta\mathbf{q}^{n+1}$ is the change in $\mathbf{q}$ during adjacent time levels and Δt is the time step. Note that the viscous terms at the right side are evaluated explicitly (at the previous time level, n) while the quantities $\mathbf{F}$ and $\mathbf{H}$ are evaluated implicitly at the new time level 'n+1'. The spanwise derivative $\delta_\eta \mathbf{G}^{*}$ is evaluated semi-implicitly, that is using old time level values and new time level values as they become available.

Equation (3) in its present form is a set of non-linear algebraic equations for the change in flow property $\Delta\mathbf{q}$. In order to solve for $\Delta\mathbf{q}$, the non-linear vectors $\mathbf{F}$ and $\mathbf{H}$ at time level 'n+1' are linearized at every time level about their values at the previous time level 'n' as follows:

$$\mathbf{F}^{n+1} = \mathbf{F}^{n} + A\ \Delta\mathbf{q} \qquad (4a)$$

$$\mathbf{H}^{n+1} = \mathbf{H}^{n} + B\ \Delta\mathbf{q} \qquad (4b)$$

where A is a 5 x 5 matrix, given by $d\mathbf{F}/d\mathbf{q}$, and B is $d\mathbf{H}/d\mathbf{q}$, evaluated at time level 'n'.

The linearized system of algebraic equations may formally be written in the following operator form, as a system of equations involving the unknown $\Delta\mathbf{q}$:

$$[I+\Delta\tau\delta_\xi A+\Delta\tau\delta_\zeta B]\{\Delta q\}^{n+1}=R^{n,\,n+1} \qquad (5)$$

where the right hand side contains known information from the previous time level about **F,G,H,R,S** and **T**. This term is called the residual. In steady state applications, a solution to the 3-D Navier-Stokes equations requires that this quantity R be driven to zero, in an iterative fashion. In an unsteady problem, R is of the order of the time step Δt and need not necessarily go to zero after several time steps.

Equation (5) couples the quantity $\Delta \mathbf{q}$ at every point in the flow field with its 4 neighbor nodes, and is a block penta-diagonal system. A direct inversion of the penta-diagonal system is costly, and some type of approximation is required to reduce the CPU time. The conventional techniques require strategies such as incomplete LU decomposition, or an alternating direction approximate factorization (AF). The AF scheme is used here, and requires factorization of the matrix operator on the left side of equation (5) into two smaller operators leading to the solution of the following equation:

$$[I+\Delta\tau\,\delta_\xi A][I+\Delta t\,\delta_\zeta B]\{\Delta q\}^{n+1}=R^{n,\,n+1} \qquad (6)$$

It may be shown that equation (6) requires solving at every node two tri-diagonal matrix equations than a single penta-diagonal matrix equation. Solution of tri-diagonal matrix systems may be performed efficiently using the well known Thomas algorithm, and may also be easily vectorized.

The above temporal differencing scheme is called a hybrid time differencing scheme, and has several advantages over fully explicit schemes and fully implicit schemes. Specifically,

a) The flow property vector q need be stored at only one time level. Most schemes require the flow properties (or changes in **q**) to be stored at several time levels. Thus, the present approach is memory efficient.

b) The above scheme requires a single evaluation of the residual at a node per time step, and two tridiagonal matrix inversions. Fully explicit schemes require residual calculations to be performed two or four times per node per time step. Fully implicit schemes require three tri-diagonal matrix inversions and are computationally expensive.

c) The present approach can be coded such that the flow variables at five η= constant planes need be in memory at a given time. Flow variables at the other planes may reside on secondary storage devices. Thus, this approach works well on virtual memory machines.

In high Reynolds number flows, the use of central differences results in odd even decoupling which can cause wriggles to appear at every time level. These high frequency spatial oscillation can grow if unchecked, and can lead to catastrophic failure of the solution and degradation of solution accuracy. To avoid this, numerical viscosity is required to damp out these oscillations. In the present work, the numerical viscosity is implemented in two different manners, namely the CD scheme and the ROE scheme.

CD scheme

The CD scheme involves the standard second order central difference discretization of the convective fluxes derivatives on the right hand side of equation (6) and the addition of a dissipation term based on the numerical viscosity model of Jameson, Turkel and Schmidt [20] as modified by Radespiel[21] to include a form of non linear isotropic characteristic speed scaling. This scaling on the dissipation term reduces excessive dissipation in cells with high aspect ratio. Such cells often inevitably result from grid clustering required in viscous flow calculation. To further enhance numerical stability, implicit dissipation with similar non-linear scaling can likewise be implemented on the left hand side of equation (6). Adding these dissipation terms, equation (6) reads

$$[I+\Delta\tau\,(\delta_\xi A-D_{I\xi})][I+\Delta t(\delta_\zeta B-D_{I\zeta})]\{\Delta q\}^{n+1} = R^{n,\,n+1}-\Delta\tau\,D_E q^n \qquad (7)$$

where $D_{I\xi}$, $D_{I\zeta}$ are second order implicit dissipation term and D_E is the explicit dissipation term made of a blend of second order and fourth order differences of the conserved variables, **q**. For example, the second order implicit and explicit dissipation terms in the streamwise direction is given by

$$D^2_{I\xi}\,q_i = [\nabla_\xi\,(\bar{\lambda}_\xi\,\varepsilon^2)_{i+1/2}\Delta_\xi]\,q_i \qquad (8a)$$

$$D_{I\xi}\,\Delta q_i = \varepsilon_I\,[\nabla_\xi\,(\bar{\lambda}_\xi)_{i+1/2}\Delta_\xi]\,\Delta q_i \qquad (8b)$$

$$\bar{\lambda}_\xi = (\lambda_\xi/J)\,[1.0+\max[(\lambda_\eta/\lambda_\xi)^\alpha,(\lambda_\zeta/\lambda_\xi)^\alpha]] \qquad (8c)$$

where ∇_ξ and Δ_ξ are the forward and backward difference operator. ε_I , ε^2 and α are user supplied constants which may be optimized to give good convergence on a given grid.

ROE scheme

Unlike the CD scheme, the ROE scheme is naturally dissipative and is best formulated as a semi-discrete finite volume representation of the convective

flux derivatives as flux balance across a cell. For example, in the streamwise direction, the right hand side of equation (6) is given by

$$\mathbf{F}_{\xi_i} = (\mathbf{F}_{i+1/2} - \mathbf{F}_{i-1/2})/\Delta\xi \qquad (9a)$$

where $\mathbf{F}_{i+1/2}$ is the flux leaving a cell (i,j,k) through the right face (i+1/2,j,k).

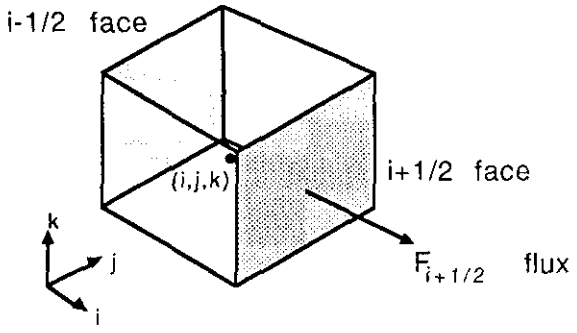

This interface flux is determined as an exact solution to an approximate Riemann wave interaction problem as developed by Roe [22] and is given by

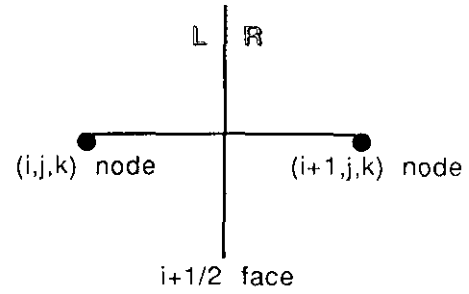

$$\mathbf{F}_{i+1/2} = 0.5[\mathbf{F}_L + \mathbf{F}_R - |\tilde{C}|(\mathbf{q}_R - \mathbf{q}_L)]_{i+1/2} \qquad (9b)$$

where $\mathbf{F}_L$ and $\mathbf{F}_R$ are the left face and right face flux of cell centered at i+1/2 node evaluated using $\mathbf{q}_L = \mathbf{q}_i$ and $\mathbf{q}_R = \mathbf{q}_{i+1}$. The dissipation contribution is given by $|\tilde{C}|(\mathbf{q}_R - \mathbf{q}_L)$ which can in turn be expanded in terms of characteristic speeds as proposed by Vinokur [23] as

$$|\tilde{C}|(\mathbf{q}_R - \mathbf{q}_L) \equiv |\tilde{C}|\Delta\mathbf{q}$$

$$= |\tilde{\lambda}_1| \begin{Bmatrix} \Delta\rho \\ \Delta\rho u \\ \Delta\rho v \\ \Delta\rho w \\ \Delta e \end{Bmatrix} + \delta_1 \begin{Bmatrix} \tilde{\rho} \\ \tilde{\rho}\tilde{u} \\ \tilde{\rho}\tilde{v} \\ \tilde{\rho}\tilde{w} \\ \tilde{\rho}\tilde{h} \end{Bmatrix} + \delta_2 \begin{Bmatrix} 0 \\ n_x \\ n_y \\ n_z \\ \tilde{U}_c \end{Bmatrix} \qquad (10)$$

$$\delta_1 = C_1 \frac{\Delta\rho}{\tilde{\rho}\,\tilde{c}^2} + 0.5 C_2 \frac{\Delta U_c}{\tilde{c}}$$

$$\delta_2 = C_1 \tilde{\rho}\,\Delta U_c - 0.5\, C_2 \frac{\Delta p}{\tilde{c}}$$

$$C_1 = -|\tilde{\lambda}_1| + 0.5(|\tilde{\lambda}_2| + |\tilde{\lambda}_3|)$$

$$C_2 = |\tilde{\lambda}_2| - |\tilde{\lambda}_3|$$

where λ_1, λ_2, λ_3 and $\tilde{U}_c$ are the characteristic speeds and contravariant velocity respectively. n_x, n_y and n_z are the unit surface normal vector components. Note that all quantities with overhead '~' are evaluated using Roe-averaged variables so that any jump in values across discontinuity is satisfied exactly according to the following relations,

$$|\tilde{C}|(\mathbf{q}_R - \mathbf{q}_L) = \mathbf{F}_R - \mathbf{F}_L$$

The above Roe flux formulation is however only first order accurate. Using pre-processing MUSCL interpolation on the primitive states variables at the interface, the order of accuracy can be formally increased. The MUSCL interpolation gives

$$(\mathbf{q}_L)_{i+1/2} = \mathbf{q}_i + 0.25\,[(1-k)\nabla\mathbf{q} + (1+k)\Delta\mathbf{q}]_i$$

$$(\mathbf{q}_R)_{i+1/2} = \mathbf{q}_i - 0.25\,[(1+k)\nabla\mathbf{q} + (1-k)\Delta\mathbf{q}]_{i+1}$$

Flux limitation on the quantities $\Delta\mathbf{q}$ and $\nabla\mathbf{q}$ can be done to ensure monotone interpolation across discontinuities like shock waves. In present work, however no flux limitation is used and a value of k=1/3 is used which corresponds to a third order accurate discretization for the flux. It is noted here that pre-processing MUSCL interpolation on Roe flux is simpler and more elegant to implement than the post-processing treatment as employed by Whitfield [13,14]. Another advantage of the Roe scheme lies in its semi-discrete finite volume representation which more accurately accounts for the metric quantities, thereby preserving the geometric conservation law.

Turbulence Modeling

The flow field over modern propellers with highly swept and twisted blades has a very viscous nature with complex features like leading edge vortices, tip vortices and secondary radial flow as reported by Bushnell [25]. Flow separation and reattachment may also be present. To capture these flow details, a viscous simulation with a suitable turbulence model is needed. In the present work, the Baldwin-Lomax turbulence model is used.

GRID GENERATION AND MOTION

A general curvilinear body fitted H-O grid is algebraically generated within the flow solver in the present calculations. Figure 1 shows the isometric view of this grid system with ξ,η,ζ (or i,j,k) in the respective streamwise, radial and azimuthal direction. For viscous calculation, it's necessary to cluster grid near the blade in the normal or azimuthal direction as seen in Figure 1. The distance of the first point from solid surface is of the order of square root of Reynold number so as to include at least a few points in the boundary layer. A grid size of 90x45x38 with 46 streamwise points and 29 radial points on blade is used in the present work.

To simulate the rotational motion of the propfan, grid motion is employed. At every time step, the whole grid system is made to rotate and advance in the same direction as the blade's motion, and the grid velocities are evaluated too. The grid velocity enters the calculations during the computations of the fluxes.

RESULTS AND DISCUSSION

The present numerical scheme has been applied to the prediction of 3-D, viscous flow field around a 2-bladed SR7L propfan. In axial flight at zero angle of attack, the flow properties do not change from one blade passage to the other. Hence, it is necessary only to solve for the flow field for a single blade passage.

Steady laminar flow and turbulent flow solution for the 2-bladed SR7L propfan, operating at 0.2 Mach number and 0.881 Advance Ratio, were obtained. The simulations were compared with experimental data [25], the inviscid prediction of Srivastava [13] and the viscous prediction of Hall [17] whenever possible.

Figure 2 and Figure 3 show respectively the comparison of the predicted chordwise variation of pressure coefficient at various spanwise locations for the hybrid CD scheme and the hybrid Roe scheme separately. It is observed consistently in these plots (Figure 2c-2e and 3c-3e) that the present results are a definite improvement over the inviscid calculation in its ability to reproduce more accurately the pressure coefficient at the trailing edge. At the leading edge, particularly so for the mid-span station, the present viscous calculation is able to capture a higher suction pressure than the inviscid calculation. However, the value still fall short from the experimental data in both laminar and turbulent flow solution. Also at the root station (Figure 2a and 3a) where Hall's data is available, the present ROE scheme's solution compares favorably with Hall's prediction and experimental data. The CD scheme however displays some oscillations and its predictions differ significantly from the experiments.

Figure 4 shows the predicted contours of pressure coefficient on the suction surface of the blade. The contours give an revealing picture of the leading edge vortex path as depicted by the region of high suction pressure bending radially outward and aftward from inboard to outboard at trailing edge near blade tip. It was found that the predicted contour of the ROE-turbulent solution resembles more accurately with the experimental data as reported in Bushnell[25] and also Hall[17] than the ROE-laminar and CD-laminar calculations.

Figure 5a to 5c give separately the particle flow trajectories and simulated oil flow patterns for the three cases. These figures were generated using the PLOT3D software. There are remarkable differences revealed in these figures among the solutions of CD-laminar, ROE-laminar and ROE-turbulent calculations. The three solutions capture the leading edge and tip vortices, but the ROE-turbulent solution more accurately reproduces the origin of the leading edge vortices near the blade root as suggested by experimental data. Radial flow patterns are also observed in all the three solutions, again more significantly in the case of ROE-turbulent solution in Figure 5c. Owing to low momentum of the fluid within the boundary layer, it is believed that the centrifugal forces will cause such radial movements. Furthermore the interaction between radial flow and leading edge vortices may also give rise to other interesting flow phenomena such as flow separation in region of adverse pressure gradient and its reattachment in region where favorable pressure gradient returns. In Figure 5c, the simulated oil flow pattern from the ROE-turbulent solution strongly suggests a region of flow separation just forward and aftward of the leading edge vortex path and also in a small section of the trailing edge near the blade tip.

Figure 6 shows the predictions of the CD scheme and ROE scheme in terms of integrated parameters of sectional lift coefficient and sectional drag coefficient under laminar consideration only. In both cases, the abrupt increase in values of C_l and C_d near the blade tip is consistent with the earlier suggestion that a strong vortical region occurs on the upper surface

slightly inboard of the tip where leading edge vortices meet with the tip vortex to form a concentrated vortex which then sweeps away into the wake. This concentration of vorticity induces higher flow velocity and lower pressure near tip region. It is also believed that the tip vortex contracts slightly in the radial direction as it gets swept into the wake during the first few revolutions. This contraction induces an upwash on the stations outboard of the tip vortex.

Figure 7 gives the predictions the elemental power coefficient and the elemental thrust coefficient across the blade span in the CD laminar and ROE laminar solution. In the comparison between the two, there is close agreement at all spanwise locations other than the tip. ROE scheme predicts consistently higher values C_P and C_T than the CD scheme at the tip.

Figure 8 show the typical convergence history of the power coefficient as a function of iteration for the CD and ROE calculations. In both instances, the C_P quantity monotonically and smoothly converge in about the same number of iterations. Both calculations were done on a HP700 series workstation using a grid size of 90x45x38. However, it should be pointed out that ROE scheme requires approximately about 0.7 minutes cpu time per iteration while the CD scheme requires about 1.0 minutes cpu time per iteration. Therefore, the ROE scheme is effectively 30% faster than the CD scheme in terms of C_P convergence to steady state.

CONCLUSIONS

An existing 3-D unsteady Euler solver has been modified to study the effects of viscosity on the performance of modern high speed propellers. In addition to the inclusion of the viscous terms, the numerical viscosity terms have been modified to use the Roe scheme or a Jameson-Turkel-Schmidt non-linear dissipation model. This has lead to a robust, stable method which gives improved results for an SR7L configuration, compared to the original inviscid analysis. Physical phenomena of interest such as the leading edge ant tip vortex formation, separation pattern and radial flow due to centrifugal pumping have been studied using this solver.

REFERENCES

1. Goldstein S., On the vortex theory of screw propellers , Royal Society Proceedings, v 123, no 792, Apr. 6, 1929, pp 440-465.

2. Sullivan J.P., The effect of blade sweep on propeller performance, AIAA paper 77-176, June 1977.

3. Egolf T.A., Anderson O. L., Edwards D.E. , and Landgrebe A.J., An analysis for high speed propeller-nacelle aerodynamic performance; Volume 1, Theory and Initial application and Volume 2, User's Manual for the computer program, United Technologies Research Center, R79-912949-19, June 1979.

4. Jou W.H., Finite volume calculation of the three dimensional flow around a propeller , AIAA paper 82-0957.

5. Hanson D.B., Compressible lifting surface theory for propeller performance calculation , AIAA paper 82-0020.

6. Williams M.H., and Hwang C., Three dimensional unsteady aerodynamic and aeroelastic response of advance turboprops, AIAA paper 86-0846.

7. Chaussee D.S., Computation of three dimensional flow through propfans, Nielsen Engineering and Research Inc., NEAR TR-199, June 1979 .

8. Chaussee D.S., Bober L. J., and Kutler., Prediction of high speed propeller flow fields using a three dimensional Euler analysis , AIAA paper 83-0188.

9. Bober L.J., Barton J. M. ,and Yamamoto O., Inviscid analysis of advanced turboprop propeller flow field , AIAA paper 85-1263.

10 Bober L.J., Yamamoto O,and Barton J. M., Improved Euler analysis of advanced turboprop propeller flow, AIAA paper 86-1521.

11 Nallasamy, Yamamoto O, Warsi S, and Bober L.J., Large Scale Advance Propeller Blade Pressure Distribution-Prediction and Data , Journal of Propulsion and Power, vol 7, no 3, 1991, pp 452-463.

12 Denton J.D., Time Marching methods for turbomachinery flow calculations, *Numerical Methods in Applied Fluid Mechanics,* edited by B.Hunt, Academic Press, 1980, pp 473-493.

13 Whitfield D.L. , Swafford T. W., Arnold A. F. S., and Belk D. M., Three dimensional Euler solution for single rotating and counter rotating propfan , AIAA paper 87-1197.

14 Janus J.M., and Whitfield D.L., Counter-rotating propfan simulation which feature a relative motion multiblock grid decomposition enabling arbitrary time step , AIAA paper 90-0687.

15 Srivastava R., and Sankar N. L., Application of an efficient hybrid scheme for aeroelastic analysis of advanced propeller , AIAA paper 90-0028.

16 Matsuo Y., Arakawa C., Saito S., and Kobayashi H., Navier-Stokes computations for flow field of an advanced turboprop , AIAA paper 88-3094.

17 Hall E. J., Delaney R. A., and Bettner J. L., Investigation of advanced counter rotating blade configuration concepts for high speed turboprop system ; Task 2, Unsteady ducted propfan analysis , Final Report , NASA CR-187106, May 1991.

18 Beam R.M., Warming R.F., An implicit factor scheme for the compressible Navier Stokes equation , AIAA journal, vol. 16, no 4, 1978.

19 Steger J.L., and Kutler P., Implicit finite differencing procedures for computation of vortex wake , AIAA journal, vol 15, no. 4, April 1977.

20 Jameson A., Schimdt W., and Turkel E., Numerical solutions of the Euler equations by finite volume methods using Runge-kutta time stepping schemes, AIAA paper 81-1529.

21 Radespiel A., Rossow C., and Swanson R.C., An efficient cell vertex multigrid scheme for the three dimensional Navier-Stokes equation , AIAA conference paper 89-1953-CP.

22 Roe, P.L , Approximate Riemann Solvers, Parameter Vectors and Difference Schemes, Journal of Computational Physics, vol 43, pp357-372, 1981

23 Vinokur M., Liu Y., Upwind Algroithms for geneneral thermochemical non-wquilibriums flow. AIAA 89-0201. 1989

24 Horlock J. H., Axial Flow Turbines-Fluid Mechanics and Thermodynamics , Robert E. Krieger Publishing company, Malabar, Florida, 1982, pp 11-13.

25 Bushnell P., Measurements of the steady surface pressure distribution on a single rotation large scale advanced numbers from 0.03 to 0.78 , NASA CR 182124, July 1988.

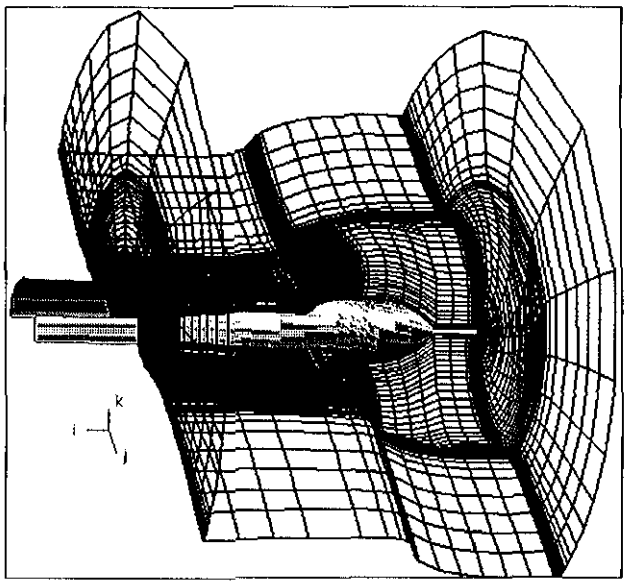

Figure 1: Isometric View of H-0 grid system

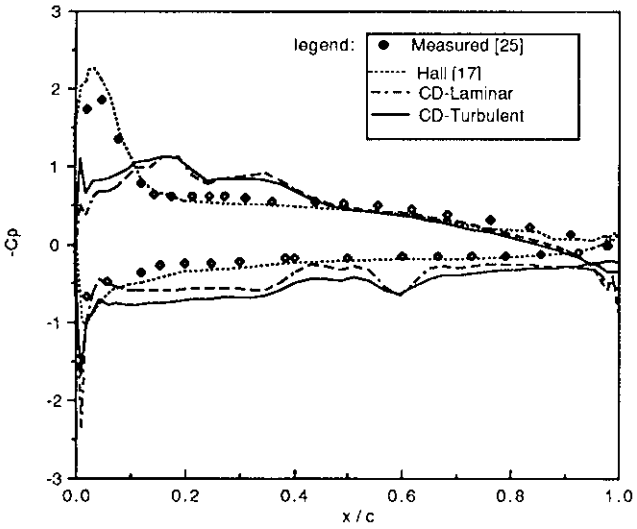

Figure 2a: Chordwise pressure distribution (CD scheme) at r/R =0.283 (Mach = 0.2 , Advance Ratio =0.881 , Beta = 31.0, Reynold No=1e6)

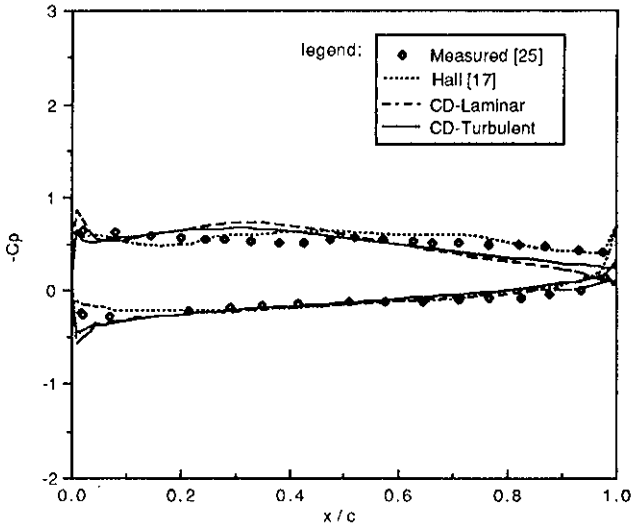

Figure 2b, cont'd : r/R=0.934

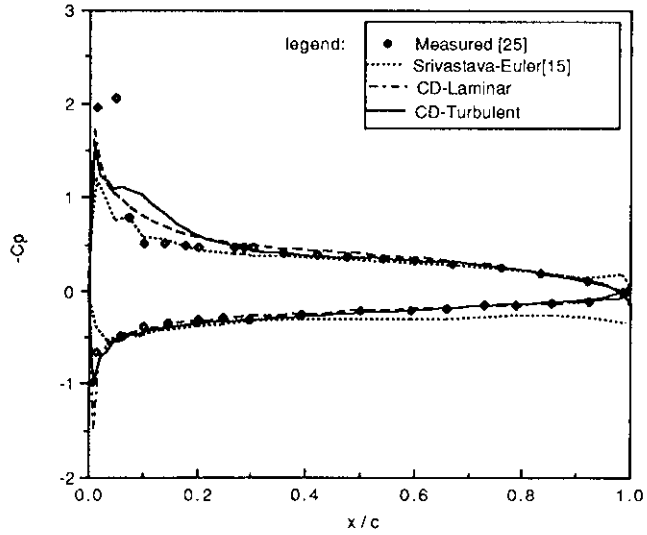

Figure 2c, cont'd : r/R=0.57

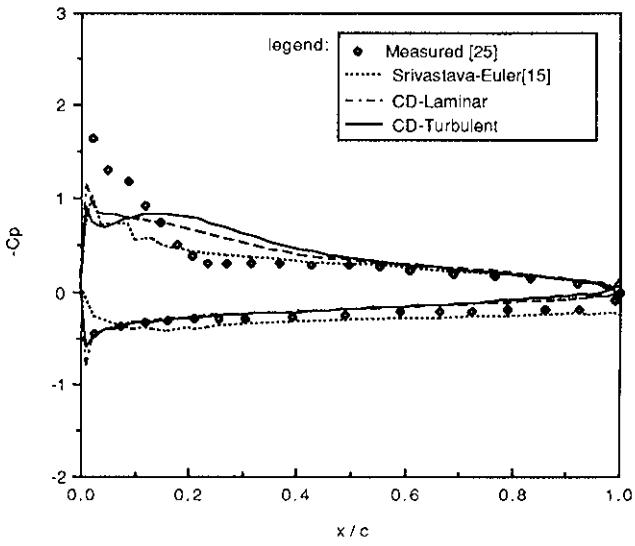

Figure 2d, cont'd: r/R=0.806

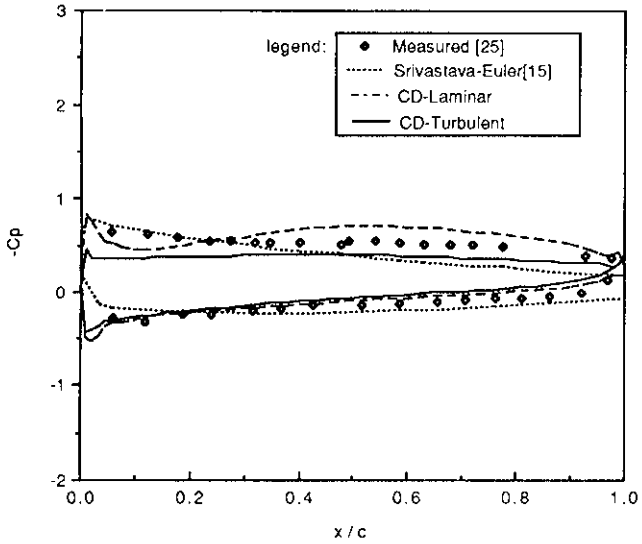

Figure 2e, cont'd : r/R=0.975

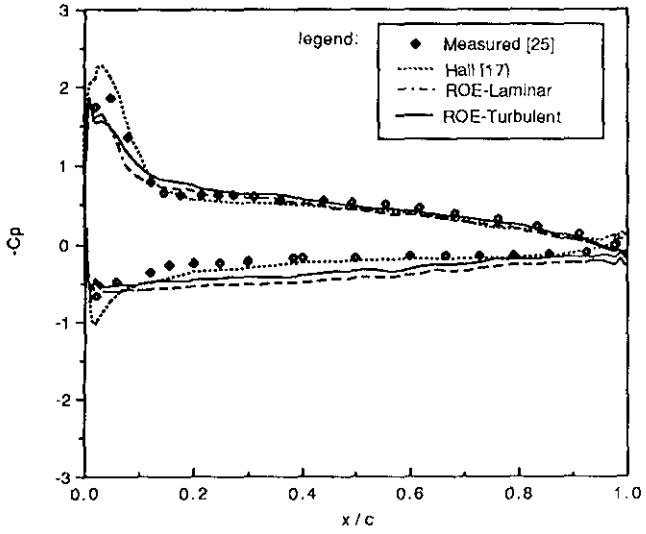

Figure 3a: Chordwise pressure distribution (ROE scheme) at r/R=0.283 (Mach No = 0.2, Advance Ratio =0.881, Beta= 31.0, Reynold No=1e6)

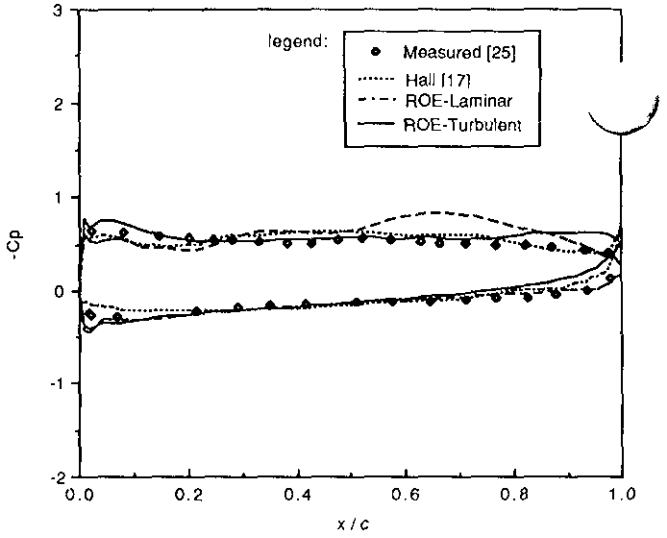

Figure 3b, cont'd : r/R=0.934

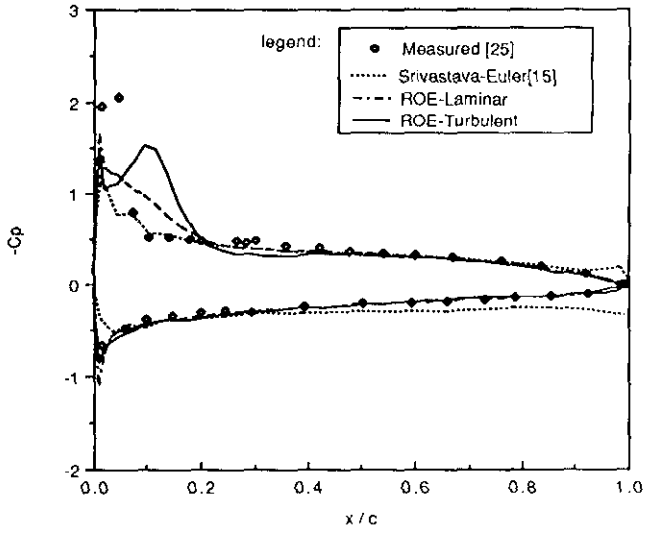

Figure 3c, cont'd : r/R=0.57

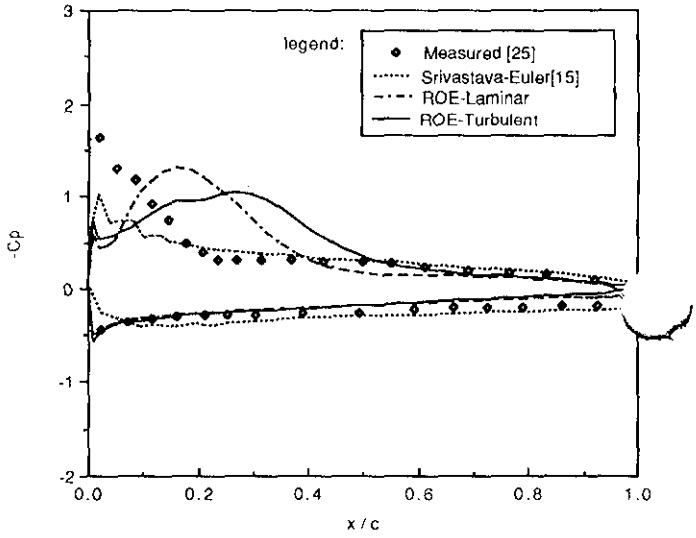

Figure 3d, cont'd : r/R=0.806

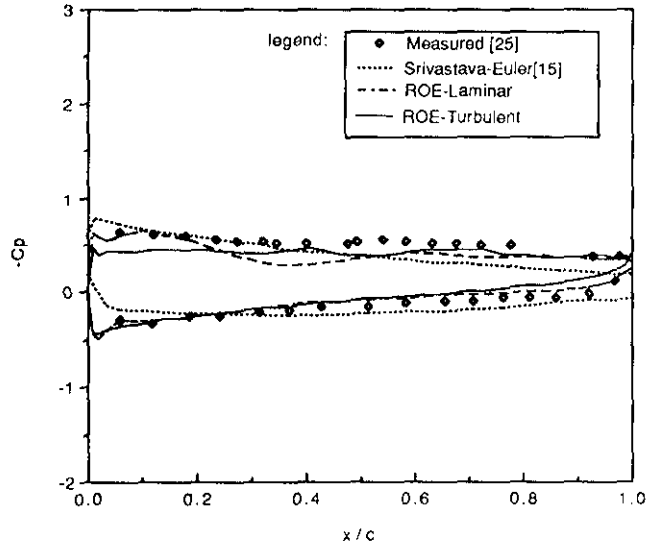

Figure 3e, cont'd : r/R=0.975

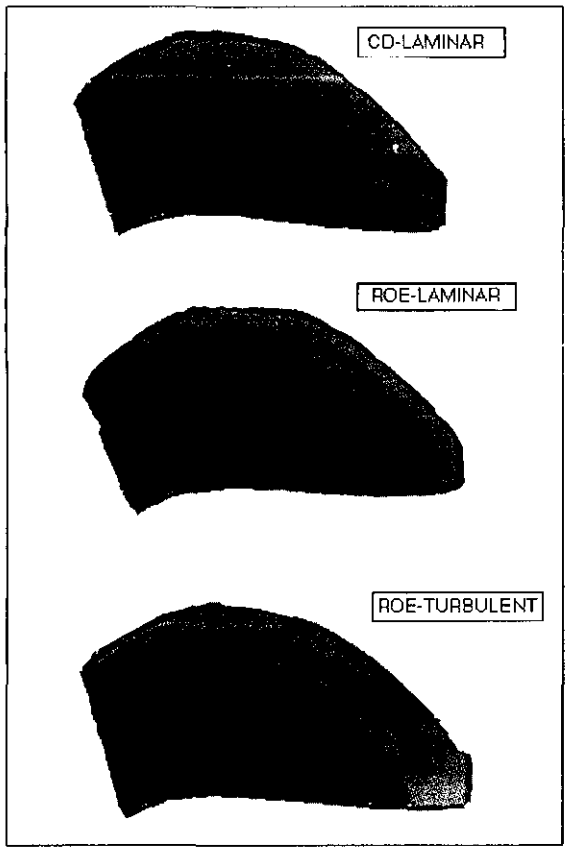

Figure 4: Contours of pressure coefficient on the suction surface of blade.

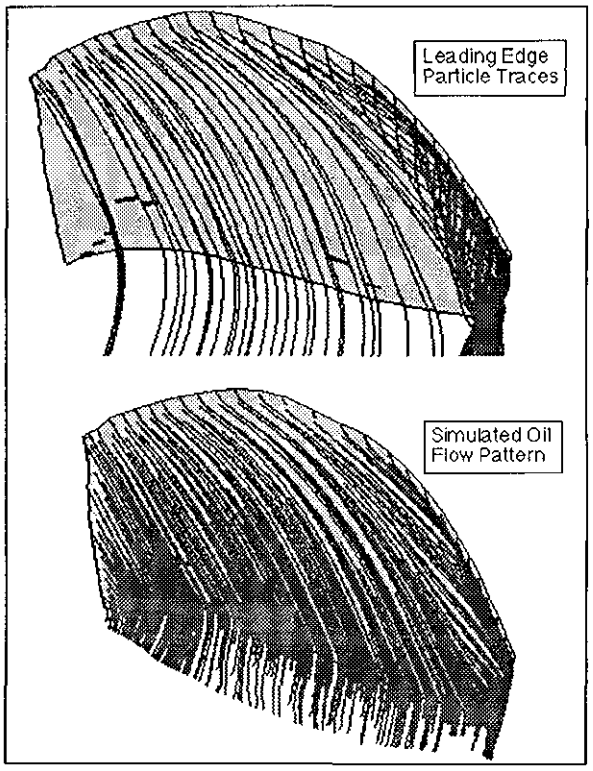

Figure 5a: Simulated flow particles trace and oil flow pattern for CD-laminar solution

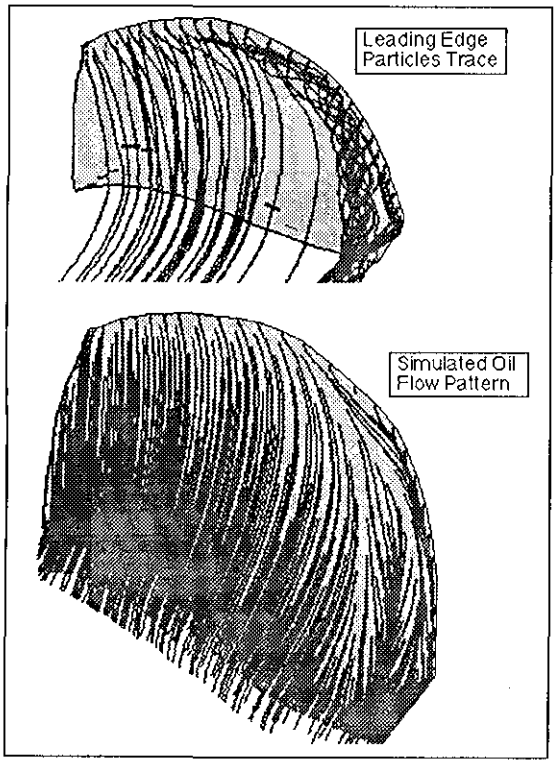

Figure 5b: Simulated flow particles trace and oil flow pattern for ROE-laminar solution

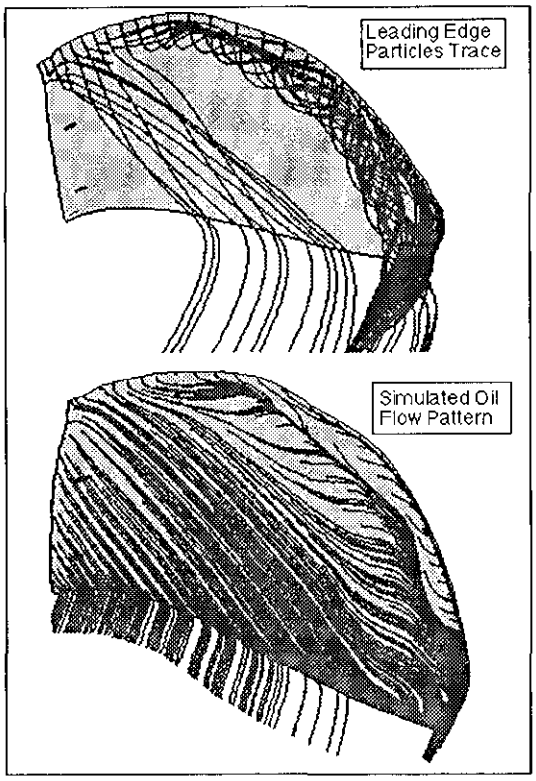

Figure 5c: Simulated flow particles trace and oil flow pattern for ROE-turbulent solution

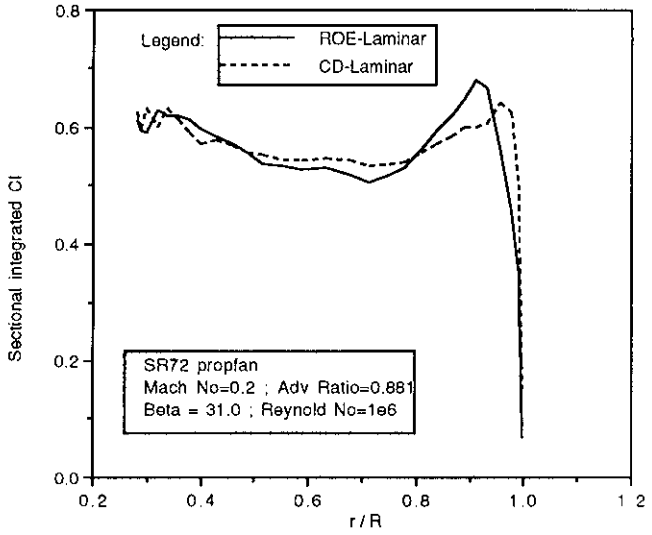

Figure 6a: Spanwise distribution of Cl coefficient

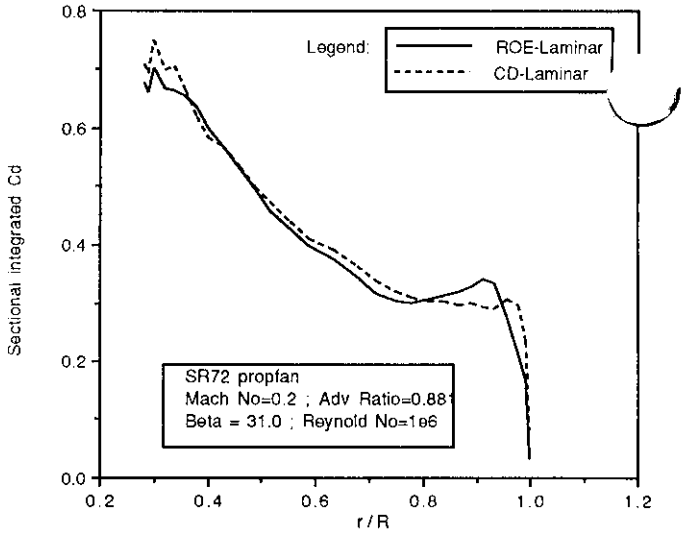

Figure 6b: Spanwise distribution of Cd coefficient

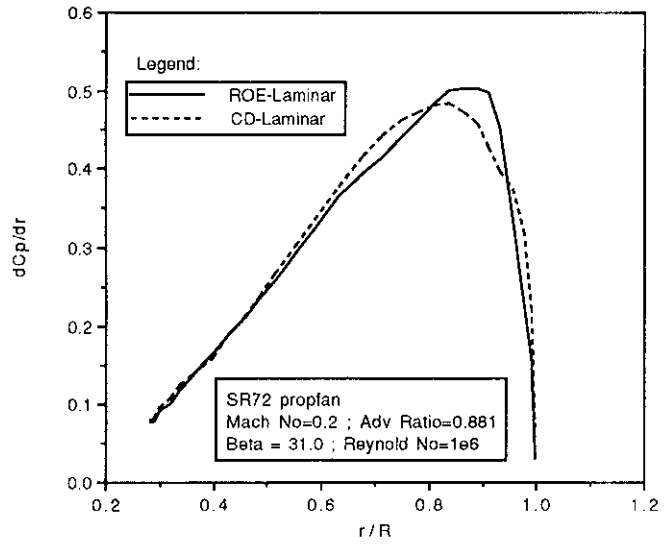

Figure 7a: Spanwise distribution of elemental power coefficient, Cp

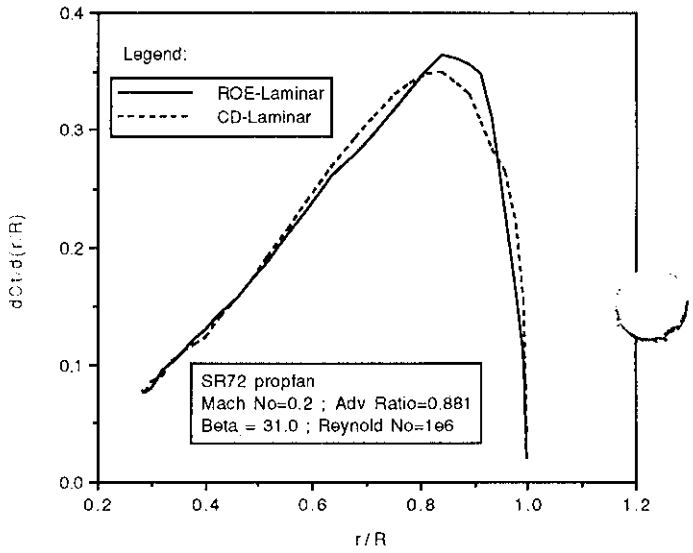

Figure 7b: Spanwise distribution of elemental thrust coefficient, Ct

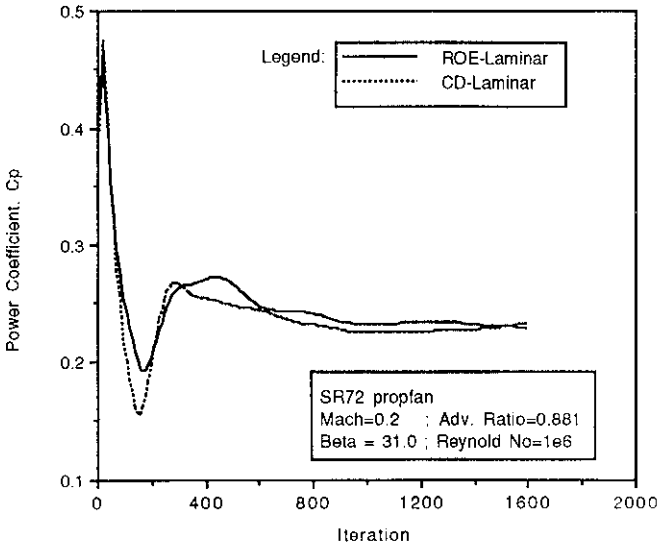

Figure 8 : Iteration History of Power Coefficient, Cp